Eleventh International Conference on Computational Fluid Dynamics (ICCFD11), Maui, HI, USA, July 11-15, 2022

ICCFD11-2022-2204

Property-Preserving Limiters for Discontinuous Galerkin Discretizations of Hyperbolic Problems

D. Kuzmin* and C. Lohmann*
Corresponding author: kuzmin@math.uni-dortmund.de

* TU Dortmund University, Institute of Applied Mathematics (LS III)
Vogelpothsweg 87, D-44227 Dortmund, Germany

Abstract: This paper presents a positivity-preserving discontinuous Galerkin (DG) method for the Euler equations. A vertex-based version of the Barth–Jespersen limiter for scalar quantities is generalized to constrain the gradients of the conservative variables in a way that ensures preservation of local bounds for the density, total energy, and pressure (internal energy). The bounds of the energy and pressure constraints are designed to become tight in regions of strong density variations and less restrictive in smooth regions. Preservation of invariant domains is guaranteed. The same methodology can be used to limit convex/concave functions of conserved variables in locally bound-preserving DG discretizations of other hyperbolic systems.

Keywords: Hyperbolic Conservation laws, Discontinuous Galerkin Methods, Slope Limiting, Local Maximum Principles, Positivity Preservation.

1 Introduction

Discontinuous Galerkin (DG) methods belong to the most popular and successful numerical schemes for computational gas dynamics. In contrast to continuous finite element approximations, they are locally conservative and local maximum principles for scalar conserved quantities are easy to enforce by limiting the gradients and/or higher-order derivatives of the finite element shape functions [6, 15, 16, 18, 19]. The bounds for the inequality constraints imposed on solution values at certain control points are commonly defined in terms of the mean values in surrounding elements. The loss of accuracy at smooth extrema can be avoided using troubled cell indicators [16, 31], WENO reconstructions [27], or hierarchical limiting techniques [15, 18, 19, 35].

In applications of DG methods to systems of conservation laws, segregated limiting of conserved quantities may fail to guarantee that other quantities of interest will stay in the range of physically admissible values. For example, the pressure may become negative causing a crash of the simulation when it comes to calculating the speed of sound. To remedy this alarming situation, positivity-preserving pressure limiters were developed for high-order discontinuous Galerkin discretizatons of the Euler equations in a number of recent publications by Zhang and Shu [38, 39]. Whereas positivity preservation is a necessary condition for obtaining physically realistic solutions, it does not guarantee the absence of spurious undershoots and overshoots in the pressure distribution. On the other hand, limiting strategies that enforce local maximum principles for derived quantities of interest [19, 29] typically rely on linearized transformations of variables and cannot guarantee positivity preservation for the pressure and internal energy. This deficiency can be cured by means of *a posteriori* corrections, as proposed in [9, 23].

In this paper, we present a positivity-preserving slope limiting procedure for DG discretizations of the Euler equations. The proposed approach was introduced in our unpublished technical report [21]. It is based on the vertex-based version [18, 19] of the Barth–Jespersen limiter [1]. In our extension to the Euler system, the energy and pressure are constrained by estimating and limiting the changes in the values of the conserved variables. The procedure for calculating the correction factors is similar to the one we developed

in the context of flux-corrected transport (FCT) algorithms for continuous finite elements [25]. The local bounds for the values of DG shape functions at the vertices of the mesh are designed to guarantee positivity of all thermodynamic variables while avoiding unnecessary limiting of the density in regions of constant pressure. A numerical study for 2D test problems demonstrates the ability of the synchronized vertex-based limiter to resolve shocks and contact discontinuities in a crisp and nonoscillatory manner.

2 DG Discretization of the Euler Equations

The Euler equations represent a hyperbolic system of conservation laws

$$\frac{\partial \rho}{\partial t} + \nabla \cdot (\rho \mathbf{v}) = 0, \tag{1}$$

$$\frac{\partial (\rho \mathbf{v})}{\partial t} + \nabla \cdot (\rho \mathbf{v} \otimes \mathbf{v} + p\mathcal{I}) = 0, \tag{2}$$

$$\frac{\partial (\rho E)}{\partial t} + \nabla \cdot (\rho E \mathbf{v} + p\mathbf{v}) = 0, \tag{3}$$

where ρ is the density, $\mathbf{v}$ is the velocity, p is the pressure, E is the total energy, and $\mathcal{I}$ denotes the identity tensor. The equation of state for an ideal polytropic gas with the heat capacity ratio γ reads

$$p = (\gamma - 1)\left(\rho E - \frac{|\rho \mathbf{v}|^2}{2\rho}\right). \tag{4}$$

The system of equations (1)-(3) can be written in the generic form

$$\frac{\partial U}{\partial t} + \nabla \cdot \mathbf{F} = 0, \tag{5}$$

where

$$U = \begin{bmatrix} \rho \\ \rho \mathbf{v} \\ \rho E \end{bmatrix}, \qquad \mathbf{F} = \begin{bmatrix} \rho \mathbf{v} \\ \rho \mathbf{v} \otimes \mathbf{v} + p\mathcal{I} \\ \rho E \mathbf{v} + p\mathbf{v} \end{bmatrix}. \tag{6}$$

The local variational problem associated with an element $T \in \mathcal{T}_h$ is given by

$$\int_T \left(w \frac{\partial U}{\partial t} - \nabla w \cdot \mathbf{F}(U) \right) \mathrm{d}\mathbf{x} + \int_{\partial T} w F_n(U_L, U_R)\, \mathrm{d}s = 0 \quad \forall w \in V, \tag{7}$$

where V is a suitably defined Sobolev space and w is a test function. The flux $F_n(U_L, U_R)$ is defined using an approximate solution to the Riemann problem with the interior state $U_L = U^+$ and exterior state $U_R = U^-$.

2.1 Boundary Conditions

On a common edge/face of two mesh elements, the states U_L and U_R are defined as the one-sided traces of the (possibly discontinuous) solution. On the boundary Γ of the computational domain Ω, the components of U_R are determined using U_L and the characteristic boundary conditions. At a supersonic inlet, $U_R := U_\infty$ is the vector of prescribed free stream values. At a supersonic outlet, we set $U_R := U_L$. On a reflecting solid wall, we reverse the sign of the normal velocity by setting $(\rho \mathbf{v})_R := (\rho \mathbf{v})_L - 2\mathbf{n}(\rho \mathbf{v})_L \cdot \mathbf{n}$. We refer to [10, 22, 34] for details and other types of boundary conditions.

2.2 Approximate Riemann Solvers

The choice of the numerical flux function F_n must guarantee consistency

$$F_n(U, U) = \mathbf{F}(U) \cdot \mathbf{n}.$$

A particularly simple formula is the local Lax-Friedrichs (Rusanov) flux

$$\mathbf{F}_n(U_L, U_R) = \frac{\mathbf{F}(U_L) + \mathbf{F}(U_R)}{2} \cdot \mathbf{n} - \max\{s_L, s_R\}(U_R - U_L), \tag{8}$$

where s_L and s_R are defined as the fastest characteristic speeds. In the case of the compressible Euler equations, the solution to the local Riemann problem is a superposition of waves moving at speeds $\mathbf{v} \cdot \mathbf{n}$ and $\mathbf{v} \cdot \mathbf{n} \pm c$, where $c = \sqrt{\gamma p/\rho}$ is the local speed of sound. Hence, we have

$$s_L = |\mathbf{v}_L \cdot \mathbf{n}| + c_L,$$

$$s_R = |\mathbf{v}_R \cdot \mathbf{n}| + c_R.$$

The Lax-Friedrichs flux (8) is very robust but tends to produce excessive numerical dissipation. As an alternative, we consider the HLL flux [14, 33]

$$F_n(U_L, U_R) = \begin{cases} \mathbf{F}(U_L) \cdot \mathbf{n} & \text{if } s_L > 0, \\ \mathbf{F}(U_R) \cdot \mathbf{n} & \text{if } s_R < 0, \\ \frac{(s_R \mathbf{F}_L - s_L \mathbf{F}_R) \cdot \mathbf{n}}{s_R - s_L} + \frac{s_L s_R}{s_R - s_L}(U_R - U_L), & \text{otherwise,} \end{cases} \tag{9}$$

where

$$s_L = \min\{\mathbf{v}_L \cdot \mathbf{n}, \mathbf{v}_R \cdot \mathbf{n}\} - \max\{c_L, c_R\},$$

$$s_R = \max\{\mathbf{v}_L \cdot \mathbf{n}, \mathbf{v}_R \cdot \mathbf{n}\} + \max\{c_L, c_R\}.$$

For a review of popular approximate Riemann solvers, we refer the reader to Toro [33].

2.3 Space Discretization

Leaving the time variable continuous for the time being, we discretize the nonlinear system (5) in space using the discontinuous Galerkin method. The vector of conserved quantities U is approximated by a linear combination of basis functions $\{\varphi_j\}$ spanning a broken Sobolev space V_h. The restriction of U_h to an element $T \in \mathcal{T}_h$ is a continuous shape function given by

$$U_h(\mathbf{x}) = \sum_j U_j \varphi_j(\mathbf{x}), \qquad \mathbf{x} \in T. \tag{10}$$

In this paper, we use rectangular meshes and linear shape functions. Thus, each component u_h of U_h is exactly represented by the Taylor polynomial

$$u_h(\mathbf{x}) = \bar{u}_T + (\mathbf{x} - \bar{\mathbf{x}}_T) \cdot \nabla u_T, \tag{11}$$

where $\bar{u}_T = u_h(\bar{\mathbf{x}}_T)$ is the cell average, $\nabla u_T = \nabla u_h|_T$ and

$$\bar{\mathbf{x}}_T = \frac{1}{|K|} \int_T \mathbf{x} \, \mathrm{d}\mathbf{x}. \tag{12}$$

The local semi-discrete problem associated with T can be written as

$$\left(w_h, \frac{\partial U_h}{\partial t} \right)_T + a_T(w_h, U_h) = b_T(w_h), \qquad \forall w_h \in V_h, \tag{13}$$

$$(w_h, U_h)_T := \int_T w_h U_h \, \mathrm{d}\mathbf{x}, \tag{14}$$

$$a_T(w_h, U_h) = \int_{\partial T} w_h F_n^+ \, \mathrm{d}s - \int_T \nabla w_h \cdot \mathbf{F}(U_h) \, \mathrm{d}\mathbf{x}, \tag{15}$$

$$b_T(w_h) = -\int_{\partial T} w_h F_n^- \, \mathrm{d}s, \tag{16}$$

where F_n^+ and F_n^- are the components of the numerical flux $F_n(U_h^+, U_h^-)$ associated with the internal and external limits of U_h on ∂T.

By (10), this local variational problem is equivalent to the linear system

$$\sum_j \frac{\mathrm{d}U_j}{\mathrm{d}t} (\varphi_i, \varphi_j)_T + \sum_j U_j a_T(\varphi_i, \varphi_i) = b_T(\varphi_i), \qquad \forall i. \tag{17}$$

The matrix form of the so-defined semi-discrete local problem reads

$$M_T \frac{\mathrm{d}U_T}{\mathrm{d}t} + A_T U_T = B_T, \tag{18}$$

where M_T is the element mass matrix, A_T is the discrete evolution operator (including the outgoing fluxes) and B_T is the vector of incoming fluxes.

2.4 Time Discretization

The semi-discrete DG scheme (18) can be discretized in time using an explicit or implicit method. In the below numerical study, we use the third-order strongly stability preserving (SSP) Runge-Kutta method [12]

$$U_T^{(1)} = U_T^n + \Delta t M_T^{-1}[B_T^n - A_T U_T^n], \tag{19}$$

$$U_T^{(2)} = \frac{3}{4} U_T^n + \frac{1}{4}\left(U_T^{(1)} + \Delta t M_T^{-1}[B_T^{(1)} - A_T U_T^{(1)}]\right), \tag{20}$$

$$U_T^{n+1} = \frac{1}{3} U^n + \frac{2}{3}\left(U^{(2)} + \Delta t M_T^{-1}[B_T^{(2)} - A_T U_T^{(2)}]\right). \tag{21}$$

This time-stepping scheme preserves the local extremum diminishing properties of the underlying space discretization under certain time step restrictions. For a presentation of other SSP Runge-Kutta methods, we refer to [11, 13].

At the end of each Runge-Kutta step, the gradients of the DG solution are constrained using the synchronized limiter presented in the next sections.

3 Limiting for Scalar Conservation Laws

Slope limiters are widely used to enforce local discrete maximum principles in finite volume and discontinuous Galerkin methods for conservation laws [1, 2, 6, 15, 29]. A typical limiting technique constrains the derivatives of a piecewise-linear or high-order approximation so as to impose some inequality constraints on the solution values at certain control points. The accuracy of the slope-limited solution depends on the location of the control points, definition of the bounds at these control points, and the algorithm used to enforce these bounds. In the context of cell-centered DG methods, vertex-based limiters [1, 18, 35] impose less restrictive constraints than procedures in which the control points are located at edge or face barycenters.

Let the bounds $u_i^{\max}$ and $u_i^{\min}$ for the value of a scalar-valued linear shape function $u_h|_T$ at a vertex $\mathbf{x}_i$ be defined as the maximum/minimum mean values in elements containing $\mathbf{x}_i$ [18]. To enforce the inequality constraints

$$u_i^{\min} \le u_h(\mathbf{x}_i) \le u_i^{\max} \tag{22}$$

at each vertex of an element T, the linear part of the shape function (11) is multiplied by a correction factor $\alpha_T \in [0, 1]$. This yields

$$\hat{u}_h(\mathbf{x}) = \bar{u}_T + \alpha_T(\mathbf{x} - \bar{\mathbf{x}}_T) \cdot \nabla u_T. \tag{23}$$

The value of α_T can be determined using the Barth-Jespersen formula [1, 18]

$$\alpha_T = \min_i \begin{cases} \min\left\{1, \frac{Q_i^{+,u}}{f_{i,T}^{(u)}}\right\} & \text{if } f_{i,T}^{(u)} > 0, \\ 1 & \text{if } f_{i,T}^{(u)} = 0, \\ \min\left\{1, \frac{Q_i^{-,u}}{f_{i,T}^{(u)}}\right\} & \text{if } f_{i,T}^{(u)} < 0, \end{cases} \tag{24}$$

where $f_{i,T}^{(u)}$ is the unconstrained linear fluctuation at the vertex $\mathbf{x}_i$, i.e.,

$$f_{i,T}^{(u)} = (\mathbf{x}_i - \bar{\mathbf{x}}_T) \cdot \nabla u_T \tag{25}$$

and

$$Q_i^{+,u} = u_i^{\max} - \bar{u}_T, \qquad Q_i^{-,u} = u_i^{\min} - \bar{u}_T \tag{26}$$

are the bounds for its constrained counterpart

$$\hat{f}_{i,T}^{(u)} = \hat{u}_h(\mathbf{x}_i) - \bar{u}_T = \alpha_T f_{i,T}^{(u)}. \tag{27}$$

An extension of this vertex-based slope limiter to higher-order DG approximations can be found in [1, 18, 19]. It is based on a representation of $u_h|_T$ in terms of Taylor basis functions and constrains the partial derivatives in a hierarchical manner using (24) to calculate a set of correction factors for the degrees of freedom associated with massless high-order terms.

4 Limiting for the Euler equations

The extension of the above vertex-based limiter to systems of conservation laws and, in particular, to the Euler equations (1)-(3) calls for the use of a common correction factor α_T for all conserved quantities. The synchronized limiting strategy should guarantee that all quantities of interest are bounded by the values corresponding to the piecewise-constant component of the DG solution. Following the procedure introduced in [25] in the context of algebraic flux correction for continuous finite elements, we consider the following system of inequality constraints for the density, energy, and pressure:

$$\rho_i^{\min} \le \rho_{i,T} \le \rho_i^{\max}, \tag{28}$$

$$\tilde{\rho}_i^{\min} E_i^{\min} \le (\rho E)_{i,T} \le \min \tilde{\rho}_i^{\max} E_i^{\max}, \tag{29}$$

$$\tilde{\rho}_i^{\min} p_i^{\min} \le \rho_{i,T} p_{i,T} = (\gamma - 1)\left[\rho_{i,T}(\rho E)_{i,T} - \frac{1}{2}|(\rho \mathbf{v})_{i,T}|^2\right] \le \tilde{\rho}_i^{\max} p_i^{\max}, \tag{30}$$

where

$$\rho_{i,T} = \bar{\rho}_T + \alpha_T f_{i,T}^{(\rho)}, \tag{31}$$

$$(\rho \mathbf{v})_{i,T} = \overline{(\rho \mathbf{v})}_T + \alpha_T f_{i,T}^{(\rho \mathbf{v})}, \tag{32}$$

$$(\rho E)_{i,T} = \overline{(\rho E)}_T + \alpha_T f_{i,T}^{(\rho E)}. \tag{33}$$

The tight bounds $\tilde{\rho}_i^{\min}$ and $\tilde{\rho}_i^{\max}$ are obtained using the scalar density limiter (see below). The remaining bounds are defined in terms of the cell averages from elements containing $\mathbf{x}_i$. The increments to be limited are given by

$$f_{i,T}^{(\rho)} = (\mathbf{x}_i - \bar{\mathbf{x}}_T) \cdot \nabla \rho_T, \tag{34}$$

$$\mathbf{f}_{i,T}^{(\rho \mathbf{v})} = \begin{bmatrix} (\mathbf{x}_i - \bar{\mathbf{x}}_T) \cdot \nabla (\rho v_1)_T \\ \cdots \\ (\mathbf{x}_i - \bar{\mathbf{x}}_T) \cdot \nabla (\rho v_d)_T \end{bmatrix}, \tag{35}$$

$$f_{i,T}^{(\rho E)} = (\mathbf{x}_i - \bar{\mathbf{x}}_T) \cdot \nabla (\rho E)_T, \tag{36}$$

where $d \in \{1, 2, 3\}$ stands for the number of space dimensions.

The choice of the correction factor α_T for the gradients of the conserved quantities must ensure that inequalities (28)–(30) hold at each vertex $\mathbf{x}_i$ of element T. The design of a failsafe limiting procedure is complicated by the strong coupling between the quantities of interest. For example, any adjustment of ρ_i may result in a violation of (30) even if $(\rho\mathbf{v})_i$ and $(\rho E)_i$ remain unchanged. Hence, changes in the values of derived quantities must be taken into account when it comes to limiting the conserved variables. In the remainder of this section, we present a synchronized limiter for enforcing (28)–(30) in the context of piecewise-linear DG approximations.

4.1 The Density Limiter

The density ρ is easy to limit and represents a natural control variable because it is discontinuous at shocks and contact discontinuities alike (in contrast to the velocity $\mathbf{v}$ and pressure p which are continuous at a contact discontinuity). For this reason, the value of the synchronized correction factor α_T should not exceed that of $\alpha_T^{(\rho)}$ such that (31) satisfies (28) for any $\alpha_T \leq \alpha_T^{(\rho)}$.

Using the Barth-Jespersen limiter (24) to calculate the correction factor

$$\alpha_T^{(\rho)} = \min_i \begin{cases} \min\left\{1, \frac{Q_i^{+,\rho}}{f_{i,T}^{(\rho)}}\right\} & \text{if } \; f_{i,T}^{(\rho)} > 0, \\ 1 & \text{if } \; f_{i,T}^{(\rho)} = 0, \\ \min\left\{1, \frac{Q_i^{-,\rho}}{f_{i,T}^{(\rho)}}\right\} & \text{if } \; f_{i,T}^{(\rho)} < 0, \end{cases} \tag{37}$$

such that the density increments $\alpha_T^{(\rho)} f_{i,T}^{(\rho)}$ are bounded by

$$Q_i^{+,\rho} = \rho_i^{\max} - \bar{\rho}_T, \qquad Q_i^{-,\rho} = \rho_i^{\min} - \bar{\rho}_T, \tag{38}$$

we define the tight bounds $\tilde{\rho}_i^{\max}$ and $\tilde{\rho}_i^{\min}$ for (29) and (30) thus:

$$\tilde{\rho}_i^{\max} = \max_T(\bar{\rho}_T + \alpha_T^{(\rho)} f_{i,T}^{(\rho)}), \tag{39}$$

$$\tilde{\rho}_i^{\min} = \min_T(\bar{\rho}_T + \alpha_T^{(\rho)} f_{i,T}^{(\rho)}), \tag{40}$$

where the maxima and minima are taken over all elements containing $\mathbf{x}_i$. The use of $\tilde{\rho}_i^{\max}$ and $\tilde{\rho}_i^{\min}$ in (29) and (30) prevents the adjustments of α_T at the energy and pressure limiting steps from smearing the density gradients in regions located far away from shocks and contact discontinuities [25].

4.2 The Energy Limiter

The second natural control variable for a synchronized FCT algorithm is the total energy. The energy bounds defined by (29) can be enforced using

$$\alpha_T^{(\rho E)} = \min_i \begin{cases} \min\left\{1, \frac{Q_i^{+,\rho E}}{f_{i,T}^{(\rho E)}}\right\} & \text{if } \; f_{i,T}^{(\rho E)} > 0, \\ 1 & \text{if } \; f_{i,T}^{(\rho E)} = 0, \\ \min\left\{1, \frac{Q_i^{-,\rho E}}{f_{i,T}^{(\rho E)}}\right\} & \text{if } \; f_{i,T}^{(\rho E)} < 0. \end{cases} \tag{41}$$

This formula constrains the energy increments $\alpha_T^{(\rho E)} f_{i,T}^{(\rho)}$ to be bounded by

$$Q_i^{+,\rho E} = \tilde{\rho}_i^{\max} E_i^{\max} - \overline{(\rho E)}_T, \qquad Q_i^{-,\rho E} = \tilde{\rho}_i^{\min} E_i^{\min} - \overline{(\rho E)}_T. \tag{42}$$

Remark. The same limiting strategy can also be used to control the components of the velocity vector $\mathbf{v}_i$. However, componentwise limiting of vector fields violates the principle of frame indifference. For this reason,

the use of frame invariant velocity/momentum limiters is recommended in [28, 37].

4.3 The Pressure Limiter

In addition to limiting the density and energy, it is essential to ensure that the pressure p does not violate the local bounds. The use of $\tilde{\rho}_i^{\max}$ and $\tilde{\rho}_i^{\min}$ in the pressure constraints defined by (30) prevents the synchronized limiter from setting the gradients of all conserved variables equal to zero in regions of constant pressure. At the same time, positivity preservation is guaranteed. Note that the bound $\tilde{\rho}_i^{\min} p_i^{\min}$ is nonnegative and $\tilde{\rho}_i^{\max} \to \rho_i$ as $\alpha_T^{(\rho)} \to 0$.

Let $\alpha_T \le \alpha_T^* := \min\left\{\alpha_T^{\rho}, \alpha_T^{(\rho E)}\right\}$ be the synchronized correction factor for the vertex-based limiter. To enforce (30), α_T should be chosen so that

$$\begin{aligned}\frac{\tilde{\rho}_i^{\min} p_i^{\min}}{\gamma-1} &\le \left(\bar{\rho}_T + \alpha_T f_{i,T}^{(\rho)}\right)\left(\overline{(\rho E)}_T + \alpha_T f_{i,T}^{(\rho E)}\right) - \frac{1}{2}\left|(\rho\mathbf{v})_T + \alpha_T \mathbf{f}_{i,T}^{(\rho\mathbf{v})}\right|^2 \\ &= \bar{\rho}_T \overline{(\rho E)}_T + \alpha_T\left(\bar{\rho}_T f_{i,T}^{(\rho E)} + \overline{(\rho E)}_T f_{i,T}^{(\rho)}\right) + \alpha_T^2 f_{i,T}^{(\rho)} f_{i,T}^{(\rho E)} \\ &\quad - \frac{1}{2}|\overline{(\rho\mathbf{v})}_T|^2 - \alpha_T \overline{(\rho\mathbf{v})}_T \cdot \mathbf{f}_{i,T}^{(\rho\mathbf{v})} - \frac{1}{2}\left|\alpha_T \mathbf{f}_{i,T}^{(\rho\mathbf{v})}\right|^2 \le \frac{\tilde{\rho}_i^{\max} p_i^{\max}}{\gamma-1}.\end{aligned}$$

Using the assumption that $\alpha_T \le \alpha_T^*$, we obtain the following estimates:

$$P_{i,T}^- \le P_{i,T} \le P_{i,T}^+, \tag{43}$$

where

$$\begin{aligned}P_{i,T} &= \alpha_T(\gamma-1)\left(\bar{\rho}_T f_{i,T}^{(\rho E)} + \overline{(\rho E)}_T f_{i,T}^{(\rho)} - \overline{(\rho\mathbf{v})}_T \cdot \mathbf{f}_{i,T}^{(\rho\mathbf{v})}\right) \\ &\quad + \alpha_T^2(\gamma-1)\left(f_{i,T}^{(\rho)} f_{i,T}^{(\rho E)} - \frac{1}{2}\left|\mathbf{f}_{i,T}^{(\rho\mathbf{v})}\right|^2\right),\end{aligned} \tag{44}$$

$$\begin{aligned}P_{i,T}^+ &= \alpha_T^*(\gamma-1)\max\left\{0, \bar{\rho}_T f_{i,T}^{(\rho E)} + \overline{(\rho E)}_T f_{i,T}^{(\rho)} - \overline{(\rho\mathbf{v})}_T \cdot \mathbf{f}_{i,T}^{(\rho\mathbf{v})}\right. \\ &\quad \left. + \alpha_T^* \max\left\{0, f_{i,T}^{(\rho)} f_{i,T}^{(\rho E)} - \frac{1}{2}\left|\mathbf{f}_{i,T}^{(\rho\mathbf{v})}\right|^2\right\}\right\},\end{aligned} \tag{45}$$

$$\begin{aligned}P_{i,T}^- &= \alpha_T^*(\gamma-1)\min\left\{0, \bar{\rho}_T f_{i,T}^{(\rho E)} + \overline{(\rho E)}_T f_{i,T}^{(\rho)} - \overline{(\rho\mathbf{v})}_T \cdot \mathbf{f}_{i,T}^{(\rho\mathbf{v})}\right. \\ &\quad \left. + \alpha_T^* \min\left\{0, f_{i,T}^{(\rho)} f_{i,T}^{(\rho E)} - \frac{1}{2}\left|\mathbf{f}_{i,T}^{(\rho\mathbf{v})}\right|^2\right\}\right\},\end{aligned} \tag{46}$$

$$Q_{i,T}^{+,\rho p} = \tilde{\rho}_i^{\max} p_i^{\max} - \bar{\rho}_T \bar{p}_T, \qquad Q_{i,T}^{-,\rho p} = \tilde{\rho}_i^{\min} p_i^{\min} - \bar{\rho}_T \bar{p}_T, \tag{47}$$

$$\bar{p}_T = (\gamma-1)\left(\overline{(\rho E)}_T - \frac{|\overline{(\rho\mathbf{v})}_T|^2}{2\bar{\rho}_T}\right). \tag{48}$$

In the estimate of the quadratic term we used the fact that

$$\alpha_T^2 \le \alpha_T \qquad \forall \alpha_T \in [0,1].$$

Introducing the vertex-based pressure correction factors

$$\alpha_{i,T}^+ = \min\left\{1, \frac{Q_{i,T}^{+,\rho p}}{P_{i,T}^+}\right\}, \qquad \alpha_{i,T}^- = \min\left\{1, \frac{Q_{i,T}^{-,\rho p}}{P_{i,T}^-}\right\} \tag{49}$$

such that

$$\alpha_{i,T}^+ P_{i,T}^+ \le Q_{i,T}^{+,\rho p}, \qquad Q_{i,T}^{-,\rho p} \le \alpha_{i,T}^- P_{i,T}^-, \tag{50}$$

we define the final synchronized correction factor α_T as follows:

$$\alpha_T = \alpha_T^* \min_i \left\{ \min\{\alpha_{i,T}^+, \alpha_{i,T}^-\} \right\}. \tag{51}$$

This limiting strategy is similar to the one developed for FCT algorithms in [25]. In contrast to the density and energy limiters, the above pressure limiter does not distinguish between positive and negative increments and tends to produce $\alpha_{i,T}^{\pm}$ smaller than necessary to enforce the local bounds.

An improved version of the synchronized limiter based on (51) can be designed using an alternative definition of the nodal correction factors $\alpha_{i,T}^{\pm}$. To determine the optimal values of $\alpha_{i,T}^{\pm}$, we consider the pressure increments

$$P_{i,T}^1 = \alpha_T^*(\gamma-1)\left(\bar{\rho}_T f_{i,T}^{(\rho E)} + \overline{(\rho E)}_T f_{i,T}^{(\rho)} - \overline{(\rho \mathbf{v})}_T \cdot \mathbf{f}_{i,T}^{(\rho \mathbf{v})}\right), \tag{52}$$

$$P_{i,T}^2 = (\alpha_T^*)^2(\gamma-1)\left(f_{i,T}^{(\rho)} f_{i,T}^{(\rho E)} - \frac{1}{2}\left|\mathbf{f}_{i,T}^{(\rho \mathbf{v})}\right|^2\right). \tag{53}$$

In the case $P_{i,T}^2 = 0$, the optimal values of $\alpha_{i,T}^{\pm}$ are given by

$$\alpha_{i,T}^+ = \begin{cases} \min\left\{1, \frac{Q_i^{+,\rho p}}{P_{i,T}^1}\right\} & \text{if } \ P_{i,T}^1 > 0, \\ 1 & \text{otherwise,} \end{cases} \tag{54}$$

$$\alpha_{i,T}^- = \begin{cases} \min\left\{1, \frac{Q_i^{-,\rho p}}{P_{i,T}^1}\right\} & \text{if } \ P_{i,T}^1 < 0, \\ 1 & \text{otherwise.} \end{cases} \tag{55}$$

In the case $P_{i,T}^2 \neq 0$, we need to solve the quadratic equation

$$\alpha_{i,T}^2 P_{i,T}^2 + \alpha_{i,T} P_{i,T}^1 = Q_{i,T}^{\pm,\rho p}. \tag{56}$$

Let

$$r_{i,T} = -\frac{1}{2}\frac{P_{i,T}^1}{P_{i,T}^2}, \qquad s_{i,T}^{\pm} = r_{i,T}^2 + \frac{Q_{i,T}^{\pm,\rho p}}{P_{i,T}^2}. \tag{57}$$

The following situations (as depicted in Fig. 1) are possible:

(a) If $P_{i,T}^1 \geq 0$ and $P_{i,T}^2 > 0$ then

$$\alpha_{i,T}^+ = \min\left\{1, r_{i,T} + \sqrt{s_{i,T}^+}\right\}, \quad \alpha_{i,T}^- = 1. \tag{58}$$

(b) If $P_{i,T}^1 \leq 0$ and $P_{i,T}^2 < 0$ then

$$\alpha_{i,T}^+ = 1, \quad \alpha_{i,T}^- = \min\left\{1, r_{i,T} + \sqrt{s_{i,T}^-}\right\}. \tag{59}$$

(c) If $P_{i,T}^1 \leq 0$ and $P_{i,T}^2 > 0$ then

$$\alpha_{i,T}^+ = \min\left\{1, r_{i,T} + \sqrt{s_{i,T}^+}\right\}, \tag{60}$$

$$\alpha_{i,T}^- = \begin{cases} \min\left\{1, r_{i,T} - \sqrt{s_{i,T}^-}\right\} & \text{if } \ s_{i,T}^- \geq 0, \\ 1 & \text{otherwise.} \end{cases} \tag{61}$$

(d) If $P_{i,T}^1 \geq 0$ and $P_{i,T}^2 < 0$ then

$$\alpha_{i,T}^- = \begin{cases} \min\left\{1, r_{i,T} - \sqrt{s_{i,T}^+}\right\} & \text{if } \ s_{i,T}^+ \geq 0, \\ 1 & \text{otherwise,} \end{cases} \tag{62}$$

$$\alpha_{i,T}^{-} = \min\left\{1, r_{i,T} + \sqrt{s_{i,T}^{-}}\right\}. \tag{63}$$

This choice of $\alpha_{i,T}^{\pm}$ guarantees that the pressure constraints are satisfied for

$$\alpha_T \leq \alpha_T^* \min\{\alpha_{i,T}^{+}, \alpha_{i,T}^{-}\}.$$

In our experience, the use of the quadratic pressure limiter leads to just marginal improvements compared to the linear version based on (49).

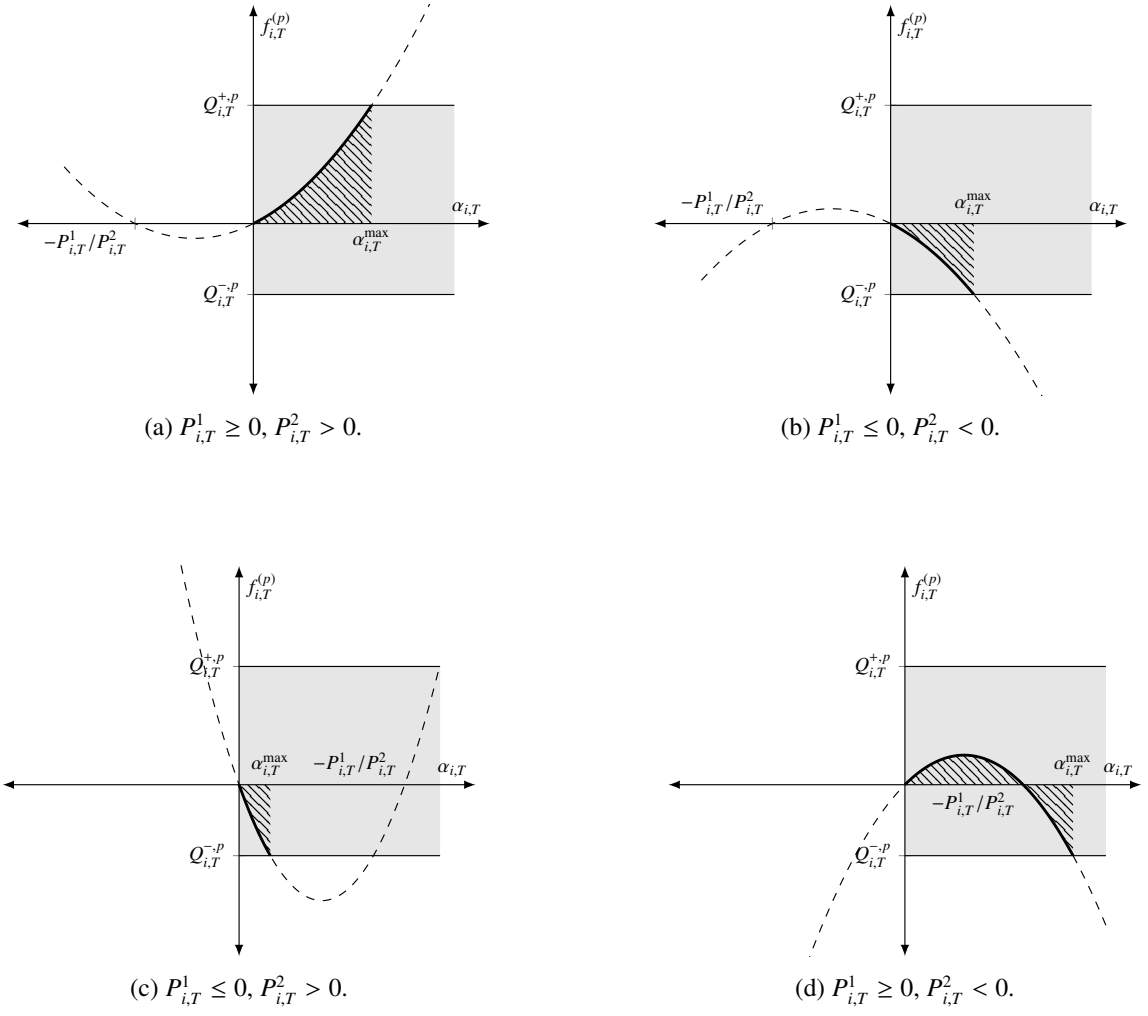

(a) $P_{i,T}^1 \geq 0$, $P_{i,T}^2 > 0$.

(b) $P_{i,T}^1 \leq 0$, $P_{i,T}^2 < 0$.

(c) $P_{i,T}^1 \leq 0$, $P_{i,T}^2 > 0$.

(d) $P_{i,T}^1 \geq 0$, $P_{i,T}^2 < 0$.

Figure 1: Roots of the quadratic equation for the pressure correction factors.

We remark that the positivity-preserving pressure limiter of Zhang and Shu [38, 39] also requires solving a quadratic equation. The main novelty of our approach is the simpler formula (49) for $\alpha_{i,T}^{\pm}$ and the definition of the local bounds for the energy and pressure in terms of $\tilde{\rho}_i^{\max}$ and $\tilde{\rho}_i^{\min}$.

4.4 Preservation of Invariant Domains

Since the local bounds of our slope limiting constraints are constructed using the cell averages of the DG-P_1 approximation, it is essential to guarantee that these cell averages stay in the convex set

$$\mathcal{G} = \{U : \ \rho(U) \geq 0, \ p(U) \geq 0\}$$

representing an *invariant domain* of the Euler system. Indeed, the use of slope-limited linear reconstructions to define the Riemann data for the numerical fluxes of the DG-P_1 discretization does not automatically imply that the DG-P_0 component is invariant domain preserving (IDP), i.e., that the output $\bar{U}_T$ of each SSP Runge–Kutta stage is in $\mathcal{G}$ if all input states are in $\mathcal{G}$. However, if the chosen numerical flux ensures this for the DG-P_0 version in 1D, the theory of IDP approximate Riemann solvers [3, 4, 5, 30] can be used to prove the corresponding result for the general case. The IDP property of vertex-based limiters for the DG-P_1 method can be shown, e.g., following the proof by Carlier and Renac [5]. A simpler alternative proof that does not involve iterative computation of pseudo-equilibrium states can be found in [20].

5 Numerical Examples

In this section, we solve standard test problems for the Euler equations using the DG scheme equipped with the proposed synchronized slope limiters.

5.1 Shock Tube Problem

Sod's shock tube problem [32] is a well-known benchmark for the Euler equations. In this numerical study, we solve it using a 2D implementation of the DG method. The computational domain $\Omega = (0,1) \times (0,1)$ has reflective walls and is initially separated by a membrane into two sections. When the membrane is removed, the gas begins to flow into the region of lower pressure. The initial condition for the nonlinear Riemann problem is given by

$$\begin{bmatrix} \rho_L \\ \mathbf{v}_L \\ p_L \end{bmatrix} = \begin{bmatrix} 1.0 \\ 0.0 \\ 1.0 \end{bmatrix}, \qquad \begin{bmatrix} \rho_R \\ \mathbf{v}_R \\ p_R \end{bmatrix} = \begin{bmatrix} 0.125 \\ 0.0 \\ 0.1 \end{bmatrix}, \tag{64}$$

where the subscripts refer to the subdomains

$$\Omega_L = (0, 0.5) \times (0,1), \qquad \Omega_R = (0.5, 1) \times (0,1).$$

The removal of the membrane at the time $t = 0$ releases a shock wave that propagates to the right with velocity satisfying the Rankine-Hugoniot conditions. All of the primitive variables are discontinuous across the shock which is followed by a contact discontinuity. The latter represents a moving interface between the regions of different densities but constant velocity and pressure. The rarefaction wave propagates in the opposite direction providing a smooth transition to the original values of the state variables in the left part of the domain. Hence, the one-dimensional flow pattern in the shock tube is characterized by three waves traveling at different speeds.

The solution profiles along the cutline $y = 0.5$ at the final time $t = 0.231$ are displayed in Fig. 2. The exact solution to Sod's shock tube problem is shown by the solid lines without markers. The solid lines with bullet markers are numerical solutions calculated using the DG method with $h = 1/128$ and $\Delta t = 10^{-3}$. The L_2 density errors (E_2^ρ) listed above the diagrams confirm that the Lax-Friedrichs flux (LF) introduces more numerical dissipation than HLL, especially in the case of the P_0 discretization (see Figs 2a,b). The difference between the slope-limited P_1 solutions is less pronounced. The results in Figs 2c,d were calculated using the scalar vertex-based limiter (labeled S) to constrain $\rho, \rho\mathbf{v}$, and ρE in a segregated manner. The unconstrained velocity and pressure exhibit undershoots and overshoots which carry over to the conserved variables. The synchronized density-energy-pressure limiter presented in Section 4 produces accurate nonoscillatory solutions, as shown in Fig. 3. The label L stands for the linear version (49) of the new pressure limiter, whereas Q refers to the limiting strategy based on solving the quadratic equation (56).

As expected, the quadratic pressure limiter produces smaller L^2 errors than its linear counterpart. However, the differences between the constrained DG approximations are marginal in this example.

5.2 Double Mach Reflection

In the second example, we consider the double Mach reflection benchmark [36] for the two-dimensional Euler equations. The computational domain for this test is the rectangle $\Omega = (0,4) \times (0,1)$. The flow pattern features a propagating Mach 10 shock in air ($\gamma = 1.4$) which initially makes a 60° angle with a reflecting wall. The following pre-shock and post-shock values of the flow variables are used to define the initial and boundary conditions

$$\begin{bmatrix} \rho_L \\ u_L \\ v_L \\ p_L \end{bmatrix} = \begin{bmatrix} 8.0 \\ 8.25\cos(30°) \\ -8.25\sin(30°) \\ 116.5 \end{bmatrix}, \qquad \begin{bmatrix} \rho_R \\ u_R \\ v_R \\ p_R \end{bmatrix} = \begin{bmatrix} 1.4 \\ 0.0 \\ 0.0 \\ 1.0 \end{bmatrix}. \tag{65}$$

Initially, the post-shock values (subscript L) are prescribed in the subdomain $\Omega_L = \{(x,y) \mid x < 1/6 + y/\sqrt{3}\}$ and the pre-shock values (subscript R) in $\Omega_R = \Omega \backslash \Omega_L$. The reflecting wall corresponds to $1/6 \le x \le 4$ and $y = 0$. No boundary conditions are required along the line $x = 4$. On the rest of the boundary, the post-shock conditions are assigned for $x < 1/6 + (1 + 20t)/\sqrt{3}$ and the pre-shock conditions elsewhere. The so-defined values along the top boundary describe the exact motion of the initial Mach 10 shock.

In Figs 4 and 5, we present snapshots of the density and pressure distribution at $t = 0.2$ calculated on a uniform mesh of 65,536 rectangular elements ($h = 1/128$) using the time step $\Delta t = 10^{-4}$. The HLL-P_0 approximation exhibits strong numerical diffusion which results in a poor resolution of the interacting shock waves. The HLL-P_1 solutions were constrained using the scalar conserved variable limiter and the synchronized density-energy-pressure limiter. The results of this 2D simulation confirm that the synchronized limiter introduces moderate amounts of numerical dissipation without generating negative pressures or spurious oscillations. Again, no significant differences are observed in the accuracy of solutions obtained with the linear and quadratic versions of the pressure limiter. This indicates that the benefit of using optimal pressure correction factors is hardly worth the effort.

6 Summary

The presented approach to synchronized limiting of the density, energy, and pressure in discontinuous Galerkin methods enforces local bounds in a way which guarantees positivity preservation while maintaining low levels of numerical dissipation. An estimate of the energy and pressure increments associated with the linear part of the DG shape functions leads to closed-form expressions for the gradient correction factors. The energy and pressure bounds for the proposed limiting procedure are designed using the scalar vertex-based limiter to determine the range of admissible values for the density. The same limiting strategy can be used to constrain antidiffusive element contributions in localized element-based FCT algorithms [7, 8].

References

[1] T. Barth and D.C. Jespersen, The design and application of upwind schemes on unstructured meshes. *AIAA Paper*, 89-0366, 1989.

[2] M. Berger, M. Aftosmis, and S. Murman, Analysis of slope limiters on irregular grids. AIAA conf., Reno, NV., Jan. 2005.

[3] C. Berthon, Stability of the MUSCL schemes for the Euler equations. *Commun. Math. Sci.* bf 3 (2005) 133–157.

[4] F. Bouchut, *Nonlinear Stability of Finite Volume Methods for Hyperbolic Conservation Laws: And Well-Balanced Schemes for Sources*. Springer Science & Business Media, 2004.

[5] V. Carlier and F. Renac, Invariant domain preserving high-order spectral discontinuous approximations of hyperbolic systems. `arXiv:2203.05452 [math.NA]`, 2022.

[6] B. Cockburn and C.-W. Shu, The Runge-Kutta discontinuous Galerkin method for conservation laws V: Multidimensional systems. *J. Comput. Phys.* **141** (1998) 199–224.

(a) LF-P_0, E_2^ρ=1.17e-3

(b) HLL-P_0, E_2^ρ=7.96e-4

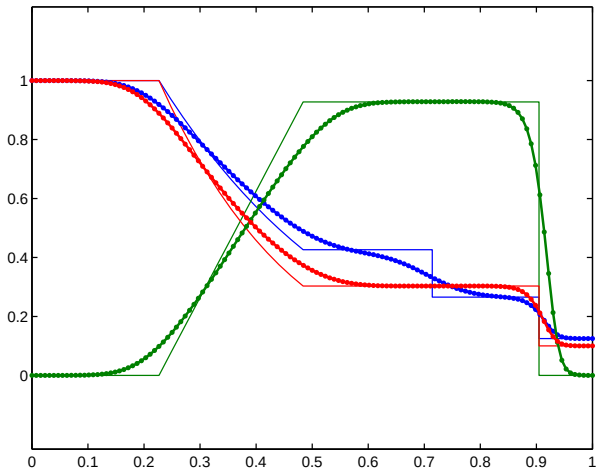

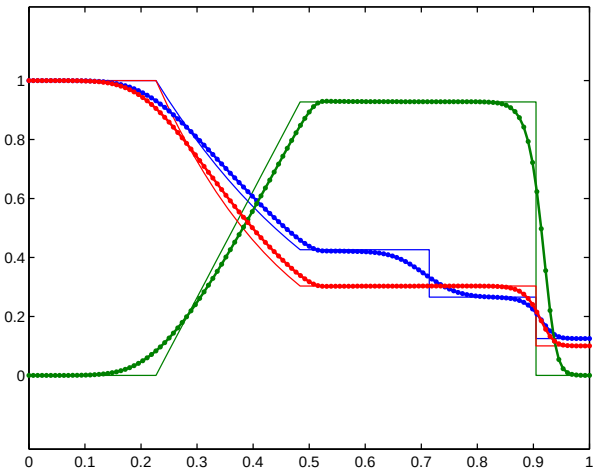

(c) LF-P_1-S, E_2^ρ=1.76e-4

(d) HLL-P_1-S, E_2^ρ=1.56e-4

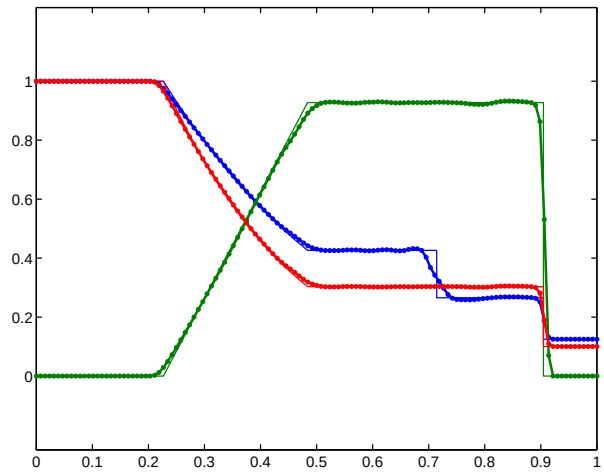

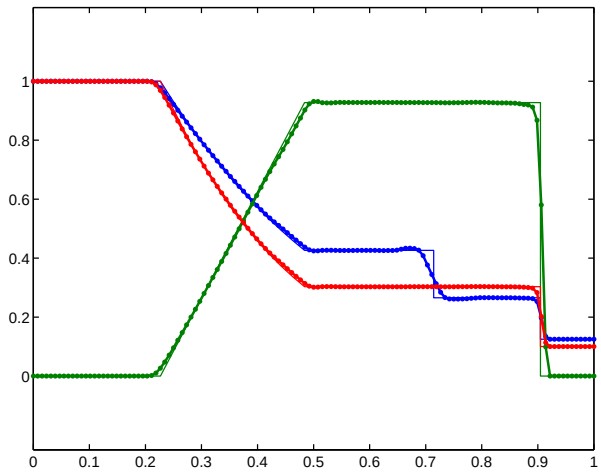

Figure 2: Shock tube problem: P_0 vs. P_1 with segregated limiting of the conserved variables, $h = 1/128$, $\Delta t = 10^{-3}$. Snapshots of the density (blue), velocity (green), and pressure (red) distribution along the line $y = 0.5$ at $t = 0.231$.

(a) LF-P_1-L, E_2^ρ=9.83e-5

(b) HLL-P_1-L, E_2^ρ=9.93e-5

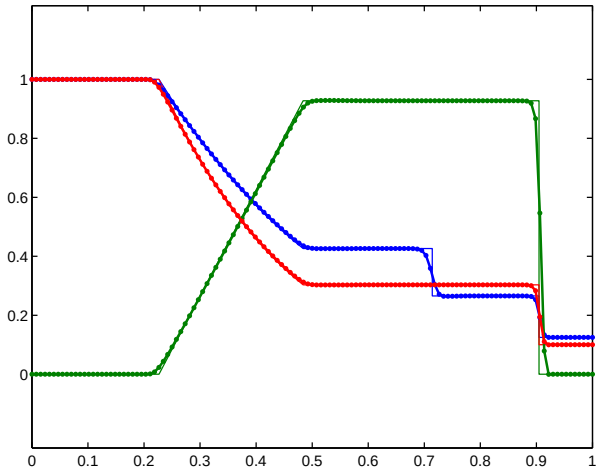

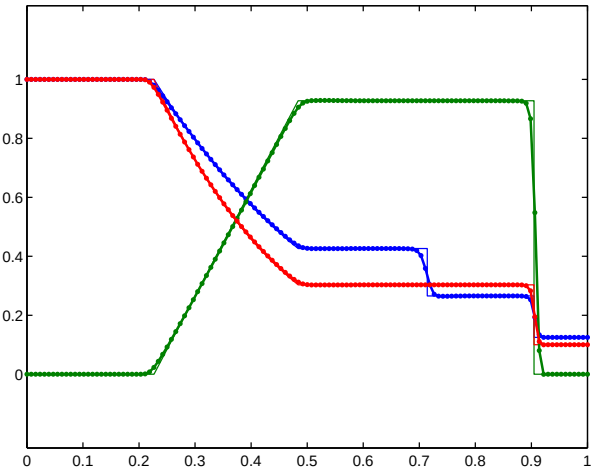

(c) LF-P_1-Q, E_2^ρ=9.61e-5

(d) HLL-P_1-Q, E_2^ρ=9.56e-5

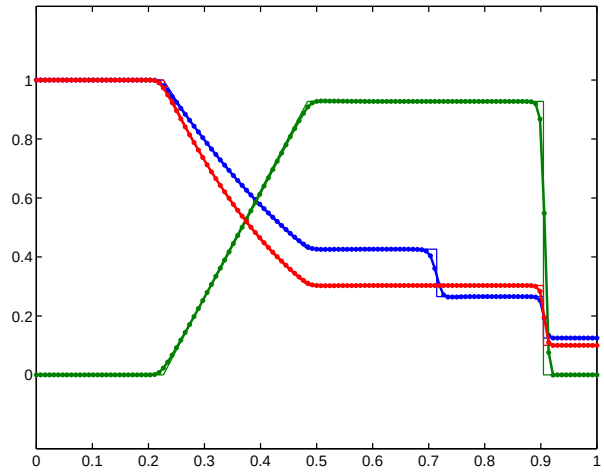

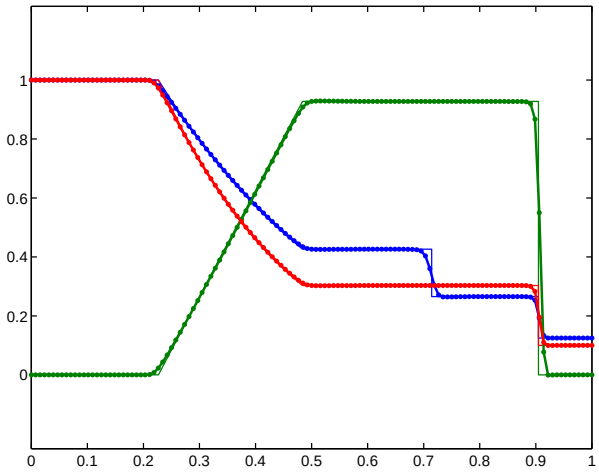

Figure 3: Shock tube problem: LF-P_1 and HLL-P_1 with synchronized limiting of the density, energy, and pressure, $h = 1/128$, $\Delta t = 10^{-3}$. Snapshots of the density (blue), velocity (green), and pressure (red) distribution along the line $y = 0.5$ at $t = 0.231$.

(a) HLL-P_0, $\rho \in [1.4, 20.60]$

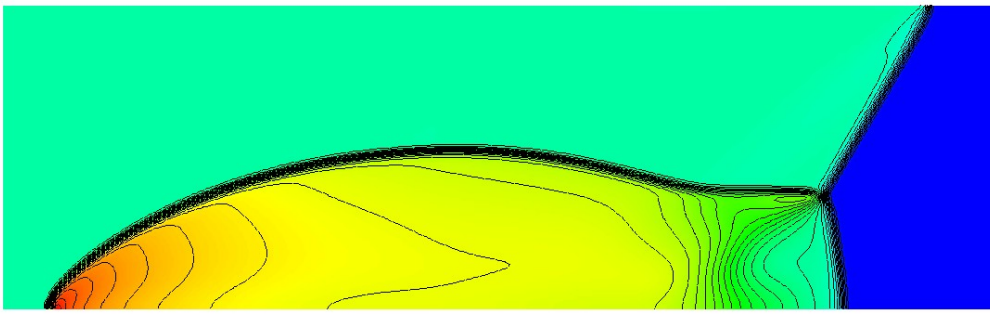

(b) HLL-P_1-S, $\rho \in [1.4, 20.56]$

(c) HLL-P_1-L, $\rho \in [1.4, 20.57]$

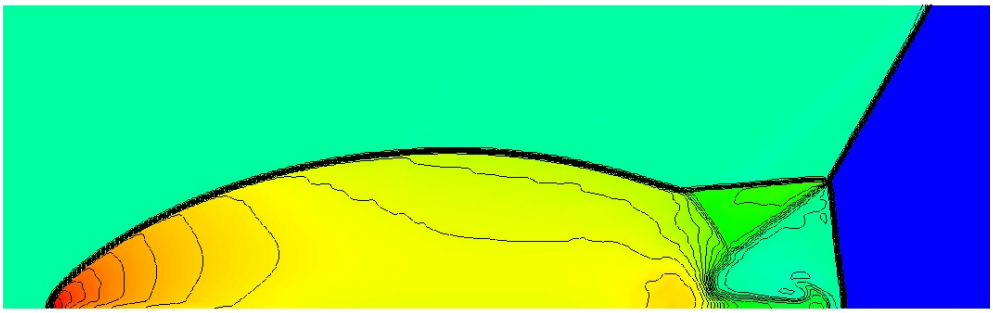

(d) HLL-P_1-Q, $\rho \in [1.4, 20.55]$

Figure 4: Double Mach reflection: density distribution at $t = 0.2$.

(a) HLL-P_0, $p \in [1.0, 544.41]$

(b) HLL-P_1-S, $p \in [1.0, 541.59]$

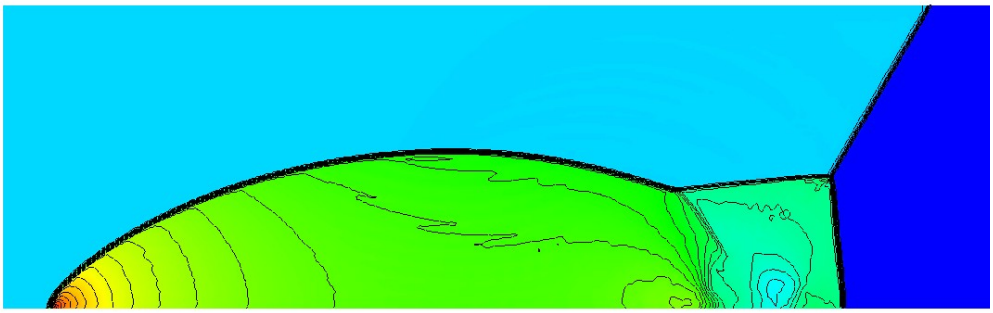

(c) HLL-P_1-L, $p \in [1.0, 543.41]$

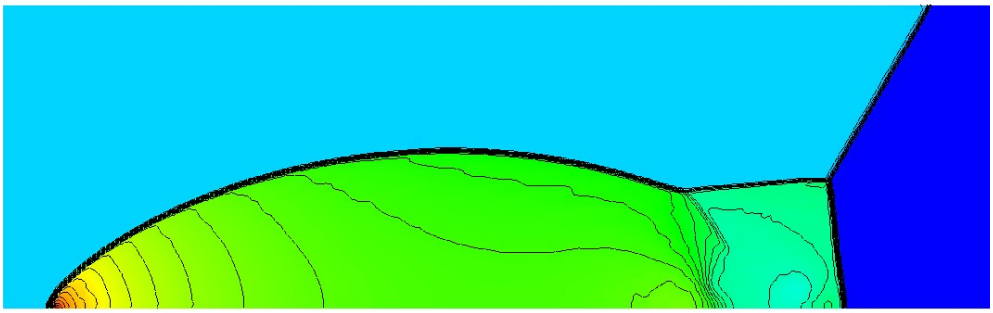

(d) HLL-P_1-Q, $p \in [1.0, 543.68]$

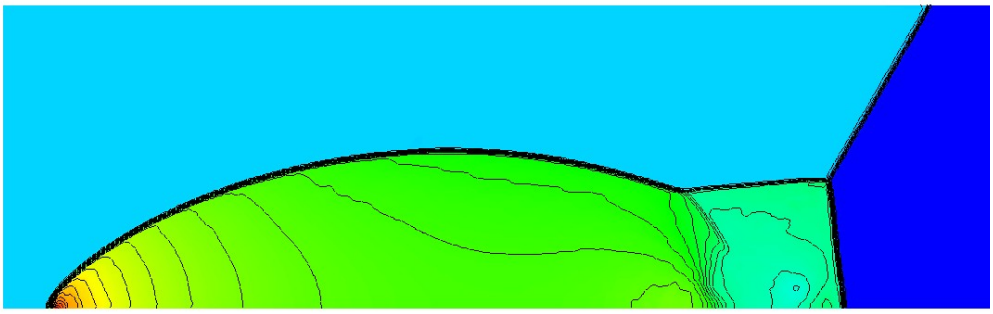

Figure 5: Double Mach reflection: pressure distribution at $t = 0.2$.

[7] C.J. Cotter and D. Kuzmin, Embedded discontinuous Galerkin transport schemes with localised limiters. *J. Comput. Phys.* **311** (2016) 363–373.

[8] V. Dobrev, Tz. Kolev, D. Kuzmin, R. Rieben, V. Tomov. Sequential limiting in continuous and discontinuous Galerkin methods for the Euler equations *J. Comput. Phys.* **356** (2018) 372–390.

[9] M. Dumbser, O. Zanotti, R. Loubère, S. Diot, A posteriori subcell limiting of the discontinuous Galerkin finite element method for hyperbolic conservation laws. *J. Comput. Phys.* **278** (2014) 47–75.

[10] M. Feistauer and V. Kučera, On a robust discontinuous Galerkin technique for the solution of compressible flow. *J. Comp. Phys.* **224** (2007) 208–231.

[11] S. Gottlieb, D. Ketcheson, C.-W. Shu, *Strong Stability Preserving Runge-Kutta and Multistep Time Discretizations*. World Scientific, 2011.

[12] S. Gottlieb and C.-W. Shu, Total Variation Diminishing Runge-Kutta schemes. *Math. Comp.* **67** (1998) 73–85.

[13] S. Gottlieb, C.-W. Shu, and E. Tadmor, Strong stability-preserving high-order time discretization methods. *SIAM Review* **43** (2001) 89–112.

[14] A. Harten, P.D. Lax and B. van Leer, On upstream differencing and Godunov type schemes for hyperbolic conservation laws, *SIAM Rev.* **25** (1983) 33–61.

[15] L. Krivodonova, Limiters for high-order discontinuous Galerkin methods. *J. Comput. Phys.* **226** (2007) 879–896.

[16] L. Krivodonova, J. Xin, J.-F. Remacle, N. Chevaugeon, and J.E. Flaherty, Shock detection and limiting with discontinuous Galerkin methods for hyperbolic conservation laws. *Appl. Numer. Math.* **48** (2004) 323–338.

[17] D. Kuzmin, Positivity-preserving extensions of the vertex-based Barth–Jespersen limiter to hyperbolic systems. In preparation for *J. Comput. Phys.* Special Issue honoring Roland Glowinski, to appear in 2023.

[18] D. Kuzmin, A vertex-based hierarchical slope limiter for p-adaptive discontinuous Galerkin methods. *J. Comput. Appl. Math.* **233** (2010) 3077–3085.

[19] D. Kuzmin, Hierarchical slope limiting in explicit and implicit discontinuous Galerkin methods. *J. Comput. Phys.* **257** (2014) 1140–1162.

[20] D. Kuzmin and H. Hajduk, *Property-Preserving Numerical Schemes for Conservation Laws*. World Scientific, to appear in 2023.

[21] D. Kuzmin and C. Lohmann, Synchronized slope limiting in discontinuous Galerkin methods for the equations of gas dynamics. Preprint, Ergebnisberichte des Instituts für Angewandte Mathematik, **541**, TU Dortmund University, 2016.

[22] D. Kuzmin, M. Möller, M. Gurris, Algebraic flux correction II. Compressible flow problems, In: D. Kuzmin, R. Löhner and S. Turek (Eds), *Flux-Corrected Transport: Principles, Algorithms, and Applications*, Springer, 2nd edition, 2012, pp. 193–238.

[23] D. Kuzmin, M. Möller, J.N. Shadid, M. Shashkov, Failsafe flux limiting and constrained data projections for equations of gas dynamics. *J. Comput. Phys.* **229** (2010) 8766–8779.

[24] R. J. LeVeque, Simplified multi-dimensional flux limiting methods. *Numerical Methods for Fluid Dynamics* **IV** (1993) 175–190.

[25] C. Lohmann and D. Kuzmin, Synchronized flux limiting for gas dynamics variables. *J. Comput. Phys.* **326** (2016) 973–990.

[26] H. Luo, J.D. Baum, R. Löhner, A Hermite WENO-based limiter for discontinuous Galerkin method on unstructured grids. *J. Comput. Phys.* **225** (2007) 686–713.

[27] H. Luo, Y. Xia, S. Li, R. Nourgaliev, C. Cai, A Hermite WENO reconstruction-based discontinuous Galerkin method for the Euler equations on tetrahedral grids. *J. Comput. Phys.* **231** (2012) 5489–5503.

[28] G. Luttwak and J. Falcovitz, Slope limiting for vectors: A novel vector limiting algorithm. *Int. J. Numer. Methods Fluids* **65** (2011) 1365–1375.

[29] S.A. Moe, J.A. Rossmanith, D.C. Seal, A simple and effective high-order shock-capturing limiter for discontinuous Galerkin methods. `arXiv:1507.03024 [math.NA]`, 2015.

[30] B. Perthame and Chi-W. Shu, On positivity preserving finite volume schemes for Euler equations. *Numer. Math.* **73** (1996) 119–130.

[31] J. Qiu and C.-W. Shu, A comparison of troubled-cell indicators for Runge–Kutta discontinuous Galerkin methods using weighted essentially nonoscillatory limiters. *SIAM J. Sci. Comput.* **27** (2005) 995–1013.

[32] G. Sod, A survey of several finite difference methods for systems of nonlinear hyperbolic conservation laws. *J. Comput. Phys.* **27** (1978) 1–31.

[33] E. F. Toro, *Riemann Solvers and Numerical Methods for Fluid Dynamics*. Springer, 1999.

[34] J.-Y. Trépanier, M. Reggio, D. Ait-Ali-Yahia, An implicit flux-difference splitting method for solving the Euler equations on adaptive triangular grids. *Int. J. Num. Meth. Heat Fluid Flow* **3** (1993) 63–77.

[35] F. Vilar, Cell-centered discontinuous Galerkin discretization for two-dimensional Lagrangian hydrodynamics. *Computers & Fluids* **64** (2012) 64–73.

[36] P.R. Woodward and P. Colella, The numerical simulation of two-dimensional fluid flow with strong shocks. *J. Comput. Phys.* **54** (1984) 115–173.

[37] X. Zeng and G. Scovazzi, A frame-invariant vector limiter for flux corrected nodal remap in arbitrary Lagrangian-Eulerian flow computations. *J. Comput. Phys.* **270** (2014) 753–783.

[38] X. Zhang and C-W. Shu, On positivity-preserving high order discontinuous Galerkin schemes for compressible Euler equations on rectangular meshes. *J. Comput. Phys.* **229** (2010) 8918–8934.

[39] X. Zhang and C-W. Shu, Maximum-principle-satisfying and positivity-preserving high-order schemes for conservation laws: survey and new developments. *Proc. R. Soc. A* **467** (2011) 2752–2776.